Thermal conductivity of GaN, ^{71}GaN, and SiC from 150 K to 850 K

Qiye Zheng,[1,*] Chunhua Li,[2] Akash Rai,[1] Jacob H. Leach,[3] David A. Broido,[2] and David G. Cahill[1]
[1]*Department of Materials Science and Engineering, Frederick Seitz Materials Research Laboratory, University of Illinois at Urbana-Champaign, 104 South Goodwin Avenue, Urbana, Illinois 61801, USA*
[2]*Department of Physics, Boston College, Chestnut Hill, Massachusetts 02467, USA*
[3]*Kyma Technologies, Inc., Raleigh, North Carolina 27617, USA*

(Received 18 October 2018; published 3 January 2019; corrected 22 July 2019)

The thermal conductivity (Λ) of wide-band-gap semiconductors GaN and SiC is critical for their application in power devices and optoelectronics. Here, we report time-domain thermoreflectance measurements of Λ in GaN, ^{71}GaN, and SiC between 150 and 850 K. The samples include bulk c- and m-plane wurtzite GaN grown by hydride vapor phase epitaxy (HVPE) and ammonothermal methods; homoepitaxial natural isotope abundant GaN and isotopically enriched ^{71}GaN layers with thickness of 6–12 μm grown on c-, m-, and a-plane GaN substrates grown by HVPE; and bulk crystals of 4H and 6H SiC. In low dislocation density ($<10^7$ cm^{-2}) bulk and homoepitaxial GaN, Λ is insensitive to crystal orientation and doping concentration (for doping $<10^{19}$ cm^{-3}); $\Lambda \approx 200$ W m^{-1} K^{-1} at 300 K and $\approx$50 W m^{-1} K^{-1} at 850 K. In ^{71}GaN epilayers at 300 K, Λ is $\approx$15% higher than in GaN with natural isotope abundance. The measured temperature dependence of Λ in GaN is stronger than predicted by first-principles based solutions of the Boltzmann transport equation that include anharmonicity up to third order. This discrepancy between theory and experiment suggests possible significant contributions to the thermal resistivity from higher-order phonon scattering that involve interactions between more than three phonons. The measured Λ of 4H and 6H SiC is anisotropic, in good agreement with first-principles calculations, and larger than GaN by a factor of $\approx$1.5 in the temperature range $300 < T < 850$ K. This paper provides benchmark knowledge about the thermal conductivity in wide-band-gap semiconductors of GaN, ^{71}GaN, and SiC over a wide temperature range for their applications in power electronics and optoelectronics.

DOI: 10.1103/PhysRevMaterials.3.014601

I. INTRODUCTION

Wide-band-gap GaN and SiC are emerging as the next-generation power semiconductors for conversion and control of electrical energy [1–3]. Owing to their high breakdown strength, electron mobility, and thermal conductivity, power devices based on GaN and SiC significantly outperform traditional Si-based devices by providing a smaller footprint, higher frequency of operation, and lower switching losses [1–4].

Thermal management is a critical factor in power devices especially when operating at high junction temperatures and output power. The device lifetime and the chip area—which in turn determine the number of dies per wafer and contribute to cost—depend on the thermal conductivity of the materials that make up the device and heat sink [5–7]. Accurate knowledge of the temperature dependence of the thermal conductivity (Λ) of GaN and SiC, as epilayers and as bulk substrates for vertical devices [8–13], is crucial for deriving scaling laws and cost models for the design of new devices.

The majority of commercially available wurtzite GaN bulk substrates are grown using hydride vapor phase epitaxy (HVPE) [14] on a foreign substrate, such as sapphire, SiC, or GaAs, which is removed after growth [15]. This method offers a relatively fast growth rate and high purity, but suffers from bowing of crystallographic planes [15–18]. More recently, the ammonothermal method has emerged as an alternative approach for the mass production of large GaN crystals [19,20]. This technique employs a polar solvent of supercritical ammonia to dissolve and recrystallize GaN on GaN seeds. Ammonothermal GaN has high crystalline quality with low dislocation density and small substrate curvature, but relatively high concentration of unintentional dopants [15,21,22]. Commercial SiC wafers are mainly grown by physical vapor transport which involves seeded sublimation at $>2000\,^{\circ}$C [23].

In GaN and SiC, heat is carried by phonons; Λ is limited by both intrinsic phonon-phonon scattering and extrinsic phonon scattering due to isotope disorder, dopants and unintentional impurities, charge carriers, point defects, and dislocations. Data for Λ of GaN and SiC with low dislocation density (10^4–10^6 cm^{-2}) at elevated temperatures, $T > 500$ K, are limited. The currently available data also show significant scatter, potentially due to differences in the sample quality but also because of the challenges that are inherent in conventional measurements of thermal conductivity at elevated temperatures. The highest Λ values were measured in free-standing thick GaN ($>100\,\mu$m) with relatively low dislocation density; the reports of room-temperature Λ of these materials range between 220 and 270 W m^{-1} K^{-1} [24–29]. In heteroepitaxial GaN/sapphire (0001) with thicknesses of 5–75 μm, Λ at room temperature varies between 110 and 195 W m^{-1} K^{-1} due to variations in dislocation densities of

*qzheng9@illinois.edu

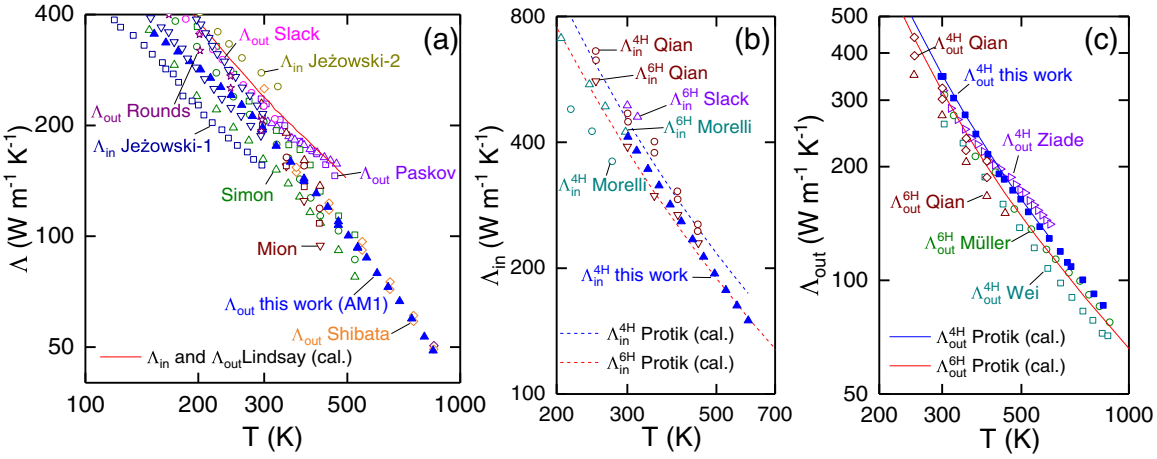

FIG. 1. (a) Thermal conductivity of bulk GaN from literature, from experiments [24–27,29,35–37], and from first-principles calculations [39], in comparison with representative results of this paper for c-plane bulk GaN (AM1) (blue solid triangles). The calculated Λ_{in} and Λ_{out} overlap with each other. (b) In-plane and (c) out-of-plane thermal conductivity of bulk 4H and 6H SiC from previous experimental [49–55] and theoretical [56] studies. Data from this paper are shown for comparison (blue solid triangles and squares).

10^7–10^{10} cm^{-2} [30–33]. In free-standing HVPE GaN, dislocation densities on the order of 10^8–10^9 cm^{-2} are reported to reduce Λ at room temperature from ≈230 W m^{-1} K^{-1} by 30–60% [34,35]. Dopants or impurities with concentrations on the order of 10^{19}–10^{20} cm^{-3} are also found to reduce Λ by ≈20–70% in ammonothermally grown bulk GaN [29,36,37].

In Fig. 1(a) we compare prior measurements of bulk GaN to our measurement of a representative bulk c-plane GaN crystal grown with the ammonothermal method. We draw two main conclusions from this comparison. At $T < 500$ K, the Λ we measured is within the range of the scattered data of highest values from prior measurements; and our Λ data in $500 < T < 850$ K is consistent with the sole prior report at these high temperatures [24]. We attribute the steep temperature dependence of Λ in [35] [dark red symbols in Fig. 1(a)] and observation of higher Λ with higher Si doping concentration in [27] [violet symbols in Fig. 1(a)] to inadequate electrical isolation between the metal line and the sample in the three-omega measurements.

Previously published reports of Λ predicted by first-principles based solution of the Boltzmann transport equation (BTE) for bulk GaN are 210–240 W m^{-1} K^{-1} along the c axis at 300 K [38–40]. These calculations predict a large isotope effect, i.e., a 50–65% increase at 300 K of Λ with isotopic enrichment of Ga [38–40]. The predicted size of the isotope effect in GaN is much stronger than the isotope effects observed in Si and Ge [41–44] and comparable to the isotope effects observed in diamond (≈50%) [45,46]. An experimental study of the effect of isotope enrichment on Λ of GaN is an important test of theory and can help evaluate the tradeoffs between costs and benefits of isotope enrichment for enhancing the thermal management of GaN-based high power devices.

In wurtzite GaN, the anisotropy in Λ, i.e., the difference between Λ_{in} along the in-plane direction (perpendicular to the c axis) and Λ_{out} along the cross-plane direction (parallel to the c axis), is relatively small at >300 K. The first-principles BTE calculations in Refs. [38,39] predict a difference between Λ_{in} and Λ_{out} of ≈1 and ≈14%, respectively, for GaN with natural abundance, and 4 and 12% in isotopically pure GaN, respectively. (In all cases, Λ_{in} at 300 K is predicted to be larger than Λ_{out}.)

There has been a growing interest in the growth of GaN in nonpolar directions, e.g., m plane (1-100) and a plane (11-20), which are free of electrostatic fields [47,48]. To the best of our knowledge, measurement of Λ of bulk m-plane GaN has not been reported previously. Such a study could resolve the discrepancy in the theoretical predictions and provide benchmark knowledge for the applications of GaN with nonpolar surface orientations.

Similar to GaN, previously reported measurements of Λ for the two common hexagonal polytypes of SiC, 4H, and 6H show significant scatter. First-principles calculations [56] predict a larger anisotropy in Λ for SiC than for GaN; at 300 K, the predicted anisotropy is ≈20 and ≈30% for 6H and 4H SiC, respectively. Figures 1(b) and 1(c) show a comparison between Λ data of 4H and 6H SiC along the in- and out-of-plane directions from literature and our measurements of 4H SiC. Λ calculated from first-principles based solution of the BTE shows better agreement with experimental results in SiC than GaN. Prior measurements of Λ_{in} at 300 K are between 390 and 490 W m^{-1} K^{-1} for 6H SiC [49,50,54,57], and between 340 and 470 W m^{-1} K^{-1} for 4H SiC [51,54]. Prior measurements of Λ_{out} at 300 K are between 270 and 310 W m^{-1} K^{-1} for 6H SiC [54,55], and between 300 and 350 W m^{-1} K^{-1} for 4H SiC [52–54]. Impurities and doping that lead to high carrier concentration (>10^{19} cm^{-3}) are found to reduce Λ by 30–50% [49–51,57].

Here, we report a time-domain thermoreflectance (TDTR) study of the temperature-dependent thermal conductivity of GaN and SiC between 150 and 850 K. We investigate low-dislocation-density bulk c- and m-plane GaN grown with HVPE and ammonothermal methods with different doping concentrations from several industrial suppliers as well as homoepitaxial layers of GaN with natural isotope abundance (referred to as GaN hereafter) and isotopically enriched ^{71}GaN (referred to as ^{71}GaN hereafter) grown on bulk c-, m-, and a-plane GaN substrates. In-plane and out-of-plane Λ of bulk semi-insulating high-quality 4H and 6H SiC are

TABLE I. Bulk GaN substrates. Sample ID, orientation, thickness, thermal conductivity at 300 K, doping type, carrier concentration (estimated by the Hall effect measurement on similar samples from the supplier, n_H, and by Raman spectroscopy of the same piece that was measured by TDTR, n_R), estimated major dopant and impurity concentration by SIMS from the supplier, XRD rocking curve FWHM, β [(002) peak for *c*-plane GaN and (100) peak for *m*-plane GaN], and dislocation density from the supplier, ρ (by CL on similar samples), and directly measured by CL (KM6) and XRD (other samples), ρ_s. The AM and XYZ samples are grown by the ammonothermal method and the rest are grown by HVPE.

Sample ID	Orientation	Thickness (μm)	$\Lambda_{300\,K}$ (W m^{-1} K^{-1})	Doping type	n_H/n_R (10^{18} cm^{-3})	Major dopant, impurity (10^{18} cm^{-3})	β (arc sec)	ρ/ρ_s (10^5 cm^{-2})
SEI	*c*	342	200	N	1.6/1.7		86	1–10/
AM1	*c*	343	197	N	0.2–2/0.6	O ≈ 1, H ≈ 1	32	≈0.5/<21
AM2	*c*	341	155	SI		Mn ≈ 15, H ≈ 20, O ≈ 5	47	≈0.5/<44
KM1	*c*	602	193	P		Mg ≈ 3	263	<100/
KM5	*m*	518	206	SI		Fe ≈ 1	166	<100/
KM6	*m*	519	203	N+	≈1/0.7	Si ≈ 0.7	166	<100/<75 (CL)
KM7	*m*	408	209	N (UID[a])	/4.0	O ≈ 0.1, H ≈ 0.1	151	<100/
XYZ	*c*	270	175	N+	10/5.4	O ≈ 10	35	/<24

[a]UID, unintentionally doped.

also reported. The crystal quality of the bulk samples is characterized by x-ray diffraction (XRD) and the dislocation density of the epilayers is estimated by cathodoluminescence (CL). The carrier concentrations in bulk GaN are estimated using Raman spectroscopy. We also perform first-principles based BTE calculations of Λ in GaN and study its dependence on mass disorder introduced by isotopes and impurities. The disagreement between experiment and theory for GaN at elevated temperatures suggests that phonon scattering processes beyond third order may be significant in GaN. This paper provides knowledge about the temperature-dependent Λ in low dislocation density bulk and homoepitaxial GaN and bulk SiC with different crystal orientations. We investigate the potential of using ^{71}GaN to achieve higher Λ.

II. EXPERIMENTAL

The bulk GaN substrates studied in this paper are provided by Kyma Technologies, Inc. (referred to below as KM); Sumitomo Electric Industries, Ltd. (SEI); Ammono (AM); and a fourth company that elected to remain anonymous (XYZ). The KM and SEI samples are grown by the HVPE method. The KM sample growth is done along the [0001] GaN crystallographic directions on *c*-plane sapphire substrates. The *m*- and *a*-plane bulk GaN are cut from thick *c*-plane boule of GaN along (1-100) and (11-20) crystal planes, respectively. The AM sample is grown by ammonothermal method as described in Ref. [20], and the XYZ sample is also ammonothermally grown. The thickness of the bulk GaN samples is 270–600 μm. The top surface of the bulk GaN substrates (Ga face of the *c*-plane samples) is prepared with chemical mechanical polishing by the suppliers. Descriptions and properties of the bulk GaN samples at room temperature are summarized in Table I.

The GaN/GaN and ^{71}GaN/GaN thick epitaxial layers provided by Kyma are grown by HVPE using natural Ga (Neo rare Metals (Utah), LL. 99.99999%, total impurity $<1.5\times10^{16}$ cm^{-3}) or isotopically enriched ^{71}Ga (Trace Sciences International, Inc. 99.6% ^{71}Ga, 0.4% ^{69}Ga, 2.6×10^{19} cm^{-3} Al, and a total of 1.2×10^{19} cm^{-3} of other metal impurity) on bulk GaN substrates including the substrates cut from the bulk wafers listed in Table I. Epilayers with *m*-plane and *a*-plane orientation are grown on Kyma HVPE GaN substrates. (These substrates are not listed in Table I.) Descriptions and properties of epilayer GaN/GaN and ^{71}GaN/GaN samples at room temperature are summarized in Table II.

Semi-insulating bulk *c*-plane 6H and 4H-SiC wafers are from TankeBlue grown by a physical vapor transport method. Both samples have a thickness of 330 μm, have a dislocation density <4500 cm^{-2}, and are doped with 1×10^{18} cm^{-3} vanadium.

A PANalytical Phillips X'pert Materials Research Diffractometers (MRD) system with a two-bounce monochromator that selects Cu $K\alpha1$ (0.15406 nm) and a PIXcel line detector is employed to perform x-ray diffraction and x-ray reflectivity (XRR) measurements. XRR is used to determine the thickness of the Al or Pt transducer layer for TDTR. (Further details of the measurement of the transducer thickness are given below.)

CL is used to measure the density of threading dislocations. For CL measurements, we use a JEOL JSM 7000F field emission scanning electron microscope (SEM) outfitted with a Gatan MonoCL3 detector with a wavelength resolution of 2 nm full width at half maximum (FWHM). The electron beam current is 0.1–3.2 nA and the beam energy is 5 kV, which yields an electron penetration depth of approximately 100 nm [58]. The same SEM is also used to measure the epitaxial GaN and ^{71}GaN layer thickness by imaging the cross section of the samples.

Raman spectroscopy measurements are performed using an Acton Insight spectrometer (Princeton Instruments). The excitation wavelength is 488 nm from a Spectra-Physics Cyan solid-state laser. The laser power is ≈3 mW. The backscattered signal is collected through a factor-20 objective (N.A. = 0.4) with laser spot size ≈10 μm at the sample surface and dispersed by a 1200-g mm^{-1} grating with a spectral resolution ≈4 cm^{-1} [59]. All Raman experiments are performed in a backscattering geometry with the incident light perpendicular to the sample surface.

TDTR is used to measure the thermal conductivity of GaN and SiC [60,61]. To remove surface contamination, especially

TABLE II. Sample ID, orientation, film thickness, thermal conductivity at 300 K, threading dislocation density (ρ_s from CL), and the substrate information of GaN/GaN with natural isotope abundance (KMF series) and ^{71}GaN/GaN (KMiF series) isotopically enriched homoepitaxial layers. All samples are grown by Kyma Technologies using HVPE with no intentional doping.

Sample ID	Orientation of substrate	Thickness (μm)	$\Lambda_{300\,K}$ (W m^{-1} K^{-1})	ρ_s (10^5 cm^{-2})	Substrate
KMF1	*c*	7.6	195		KM (SI)
KMF2	*c*		203	<10	AM1
KMF3	*c*		203	<40	SEI
KMF4	*c*	8	194	<10	AM2
KMF5	*m*	6.4	153		KM
KMF6	*c*		190	<50	KM (N-type)
KMiF1	*c*		237		AM2
KMiF2	*c*	8	240	<400	KM (UID)
KMiF3	*c*		246	<60	AM1
KMiF4	*a*	11.6	234	<200	KM (N-type)
KMiF5	*m*	7.6	218	<60	KM (N-type)
KMiF6	*c*	7.5	240		KM (SI)
KMiF7	*c*	7	233	<20	SEI

hydrocarbons, the samples are first cleaned by O_2 plasma under 18-W rf power at 500 mTorr for 80 s using a Harrick PDC-32G Basic Plasma Cleaner. The samples are then transferred to a vacuum chamber (within 5 min) and coated with an Al or Pt transducer layer with a thickness of approximately 80 or 60 nm, respectively, by dc magnetron sputtering. Aluminum thin films are used for measurements in the range $150 < T < 600$ K; Pt thin films are used for measurements at high temperatures up to 850 K. The O_2 plasma treatments are found to be effective for generating a consistent interface thermal conductance of $180 < G < 230$ MW m^{-2} K^{-1} for both Al/sample and Pt/sample interfaces at room temperature. For temperature-dependent measurements, samples are mounted on an Instec vacuum microscope stage using PELCO graphite paint. The stage chamber is pumped with a turbomolecular pump to maintain a pressure within the vacuum stage of $<8 \times 10^{-4}$ Torr. The measurement for SiC along the in- and out-of-plane direction is performed on the cleaved cross section and polished top surface, respectively. On the cleaved surfaces, we select an area of the sample surface with an optical reflectivity >95% of the optical reflectivity of a silicon wafer coated with the same transducer metal. Specular surfaces are needed to avoid artifacts in the TDTR measurements that are sometimes generated by thermoelastic modulation of diffuse light scattering.

In a TDTR measurement, a train of 785-nm optical pulses at a repetition rate of 74.86 MHz, generated by a mode-locked Ti:sapphire laser, is split into pump and probe beams with the optical path of the pump beam controlled by a mechanical delay stage [60,61]. The pump beam is modulated at a frequency of $f = 9.3$ MHz by an electro-optical modulator. The pump and probe beams are typically focused on the sample through a factor-5 objective lens to a $1/e^2$ intensity radius of $w_0 \approx 10.2\,\mu$m. Objective lenses with magnification larger and smaller than factor 5 are used to determine the dependence of the apparent thermal conductivity on the laser spot size. The steady-state temperature rise created by the average laser beam power of 25 mW is $<0.01\,T$ for all measurements. Changes in the intensity of the reflected probe beam due to the thermoreflectance of the Al transducer and pulsed heating created by the pump beam are measured using lock-in detection. The ratio of the in-phase (V_{in}) and out-of-phase (V_{out}) signal from the lock-in amplifier is then fit to a thermal diffusion model obtained from an analytical solution for heat flow in a layered structure based on Fourier's law [60].

The diffusive thermal transport model used for TDTR data fitting includes parameters for the thermal conductivity Λ, heat capacity C_P, and thickness of the metal transducer and the sample (GaN, ^{71}GaN or SiC) as well as the thermal conductance of the transducer/sample interface (and the GaN/GaN or ^{71}GaN/GaN interface for epilayer samples). The accuracy of the Λ measurement is estimated by calculating the square root of the sum of the squares of errors propagated from uncertainty in each parameter of the model as well as the phase difference between the thermoreflectance signal and the reference channel input to the lock-in amplifier [62]. We define the sensitivity of the fit S_α as the logarithmic derivative $-V_{in}/V_{out}$ with respect to each of the parameters α, i.e., $S_\alpha = \frac{\partial \ln(-V_{in}/V_{out})}{\partial \ln(\alpha)}$, to gauge how each parameter influences the output of the model. For example, the typical sensitivity for Λ of GaN is $\approx$0.5 at >300 K, which means that a 10% change in the Λ results in 5% change in the ratio signal. The error from measurement uncertainty σ_α for a parameter α that propagates into the measured Λ is then $\sigma_\alpha S_\alpha / S_\Lambda$. The typical measurement uncertainty of Λ is approximately 7%.

Since all epitaxial GaN and ^{71}GaN layers in this paper have thickness >6 μm, thicker than the maximum TDTR thermal penetration depth $d_p = \sqrt{\Lambda/(\pi f C_P)} \approx 3\,\mu$m reached at 150 K, the GaN/GaN (^{71}GaN/GaN) interface thermal conductance is not detected (sensitivity <0.001). Consistent with prior work on a wide variety of single crystals [63,64], we do not observe modulation frequency dependence in the apparent thermal conductivity when we change the modulation frequency in the range $1.1 < f < 9.3$ MHz.

With a relatively large laser spot size of $w_0 \approx 10.2\,\mu$m, the TDTR measurement is insensitive to heat transfer in the in-plane direction. For GaN, the maximum sensitivity to Λ along the direction parallel to the sample surface (which occurs at

the lowest temperature of 150 K) is <0.1. Since the difference between Λ_{in} and Λ_{out} is <5% at all temperatures according to our first-principles calculation, we ignore the anisotropy of Λ in the analysis. In TDTR analysis of c-plane GaN, changing the anisotropic ratio of $\Lambda_{in}/\Lambda_{out}$ from 1 to 1.14 (the ratio in [38]) at 150 K only leads to ≈2% difference in the fitting result of Λ_{out}. This is smaller than the typical measurement uncertainty of approximately 7%. The difference becomes negligible at higher temperature, <1% at >300 K.

In SiC, Λ_{in} is ≈28% larger than Λ_{out} at 300 K according to first-principles calculations [56]. For 4H SiC, changing the ratio of Λ_{in} and Λ_{out} from 1 to 1.28 would cause the fitting result of Λ_{out} measured from the top surface and Λ_{in} from the cross section to change by ≈3% at 300 K. The difference becomes smaller at higher temperature. Considering the small effect of anisotropy on the analysis of the TDTR data for 4H and 6H, we treat Λ as isotropic in the analysis.

The thickness of the Al thin film is obtained from picosecond acoustics using a longitudinal speed of sound 6.42 nm ps^{-1} [65] which is consistent with x-ray reflectivity measurement within 2%. A small correction to the Al film thickness in the TDTR analysis is made by adding an extra 3 nm to the thickness derived from picosecond acoustics to account for the heat capacity of a layer of native oxide. The Λ of the Al thin film is calculated using the Wiedemann-Franz (W-F) law and the electrical resistance of the Al film deposited on a 500-nm SiO_2 on Si reference sample placed next to the sample during sputtering. Λ values for Al at temperature different from 300 K are estimated from the electrical resistivity at 300 K, the assumption of a constant residual resistivity added to the intrinsic electrical resistivity, and the W-F law [66] with a constant Lorenz number. The analysis is relatively insensitive to the Al transducer layer thermal conductivity [62]. The heat capacity of Al is taken from literature values [67]. For Pt transducers, the film thickness is measured by x-ray reflectivity. The Λ of Pt is also derived from electrical resistivity and the W-F law [68], similar to Al. The heat capacity of Pt is taken from [69]. The thermal expansion of the transducer layers is also considered (see Supplemental Material [70]).

The volumetric heat capacity at constant pressure of GaN and SiC, C_p, is calculated using $C_p = C_v + \alpha^2 BT$, where C_v is the constant volume heat capacity, B is the bulk modulus, and α is the volumetric thermal expansion coefficient. C_v is obtained by integrating the phonon density of states (DOS) derived from our first-principles calculations. We use experimental values of B for GaN [71] and SiC [72] and α (derived from $\alpha = 2\alpha_a + \alpha_c$) for GaN [73] and SiC [74,75]. As shown in Fig. S1 in Supplemental Material [70], the calculated C_p of GaN is in good agreement with the measurement results by Kremer *et al.* [76] between 150 and 850 K with deviation of less than 3% while the calculated C_p of 6H and 4H SiC agrees well with prior work [77–82]. We note that the experimental data of C_p for GaN [83–89] show relatively large deviations. The difference in C_p between ^{71}GaN and GaN is negligible above 150 K [76].

For TDTR measurements of high thermal conductivity crystals, we must consider deviations from Fourier's law [63,64]. Such deviations result from ballistic phonon transport in the sample and from a mismatch in the distribution of phonons that carry heat across the metal transducer/sample interface and the distribution of phonons that carry heat in the sample. A reduction in the characteristic length scales of the temperature gradient by decreasing the laser spot size (w_0) or increasing the pump modulation frequency (f) increases the percentage of low-frequency phonons with long mean free paths that are not in local equilibrium with high-frequency phonons. Such effects cause the apparent thermal conductivity (Λ_A) derived from the thermal model using a small characteristic length scale to be less than the apparent thermal conductivity derived from the thermal model using a large characteristic length scale [63]. The laser spot size dependent Λ_A for representative GaN and SiC samples at room temperature is shown in Fig. S2 in Supplemental Material [70]. For GaN, ^{71}GaN, and SiC, the difference between Λ_A measured with $w_0 = 10.2$ and 30 μm is ≈2–5%, smaller than the typical uncertainty of TDTR measurements.

The first-principles lattice thermal conductivity is computed using an iterative solution of the phonon Boltzmann transport equation (PBE), the details of which can be found in previous publications [90,91]. This approach requires the *ab initio* calculation of the harmonic and anharmonic interatomic forces (IFCs). Harmonic IFCs are calculated within the local density approximation and using density functional perturbation theory (DFPT) as implemented in QUANTUM ESPRESSO [92]. We use the ultrasoft pseudopotentials by Garrity *et al.* [93] with a plane-wave cutoff of 60 Ry and a charge density cutoff of 300 Ry. A $20 \times 20 \times 10\,\mathbf{k}$ grid and a $5 \times 5 \times 5\,\mathbf{q}$ grid are used in the DFPT calculations. The crystal structures are determined by minimizing the free energy in the quasiharmonic approximation at each temperature. Thus, both the zero-point motion of the atoms and thermal expansion are included. This yields the 300-K lattice constants and internal parameter as $a = 3.1653$ Å, $c = 5.1618$ Å, and $u = 0.3767$. The lattice constants are within 1% of measured room-temperature values [94]. The anharmonic IFCs were calculated using a supercell/finite difference scheme [95]. Forces are calculated in a 108-atom supercell with a $2 \times 2 \times 2\,\mathbf{k}$ grid. Anharmonic IFCs up to the sixth-nearest neighbors are retained. The phonon frequencies, phonon eigenmodes, and three-phonon scattering rates are then computed from the harmonic and anharmonic IFCs, and the PBE is solved on a $30 \times 30 \times 30\,\mathbf{q}$ grid, which is sufficient to obtain converged thermal conductivity values. The phonon-isotope scattering is modeled within the mass variation approximation as formulated by Tamura [96].

III. RESULTS AND DISCUSSION

Figures 2(a) and 2(b) show representative x-ray rocking curves (ω scan) for symmetrical reflections of bulk c- and m-plane GaN. The HVPE samples (black lines) with both c- and m-plane orientation show broader FWHM than the ammonothermal samples (blue lines). The significant curvature of free-standing GaN grown by HVPE on foreign substrates and the relatively high dislocation density lead to the broadening of XRD rocking curves in HVPE GaN compared with ammonothermal samples (see Table I) [17,18]. The FWHM of the rocking curves in ammonothermal c-plane GaN are on the same order of magnitude as that of the (004) peak of Si single crystal wafer, 18 arc sec, comparable to the XRD instrumental

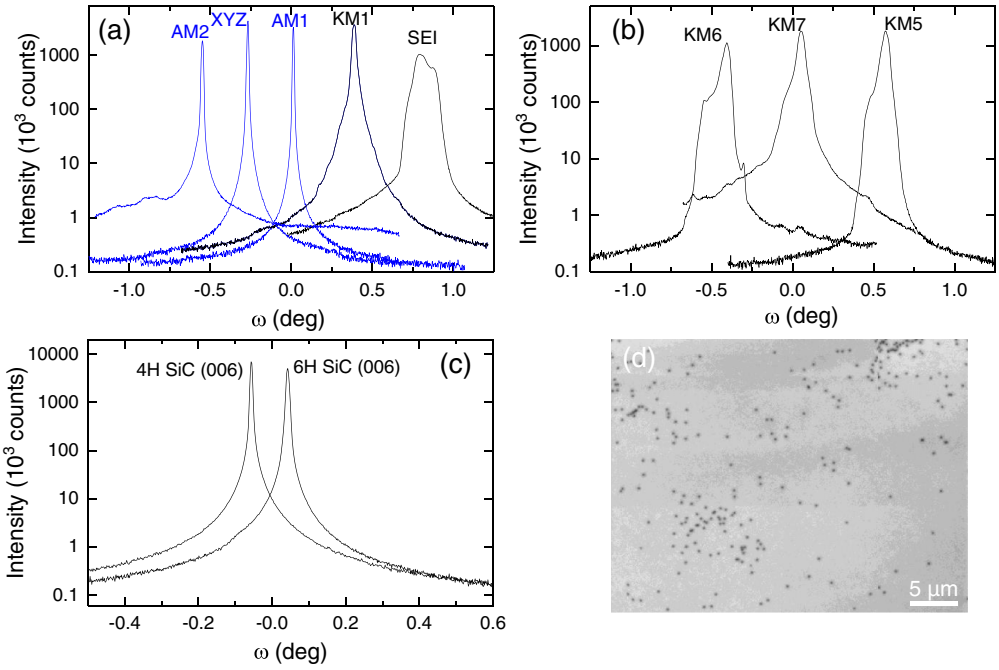

FIG. 2. XRD rocking curves of (a) c-plane [(002) peak] and (b) m-plane [(100) peak] bulk GaN grown by HVPE (black lines) and ammonothermal method (blue lines). The curves are shifted along the ω axis for better visibility. (c) XRD rocking curve of 4H and 6H SiC (006) peaks. (d) Representative cathodoluminescence of the ^{71}GaN epilayer of KMiF2 with dark spots corresponding to the locations of threading dislocations.

broadening. The FWHM of the 4H and 6H SiC (006) rocking curves are also small, ≈21 arc sec, consistent with the low dislocation density of around 4500 cm^{-2} specified by the supplier.

With radius of curvature on the order of 10^2–10^3 m [17], the tilt and twist of mosaic crystals in ammonothermal GaN can be correlated with dislocation densities. The tilt of (001) oriented GaN layers can be correlated to the density of screw-type threading dislocations (TDs) with Burgers vector $\boldsymbol{b}_s = \langle 0001 \rangle$ (with magnitude $b_s = 0.5186$ nm) [97,98]. Assuming the geometric misfit to be compensated by screw-type TDs which are randomly distributed, the screw-type TD density is given by [97,99]

$$\rho_s = \frac{\beta^2}{4.53 b_s^2} \tag{1}$$

where β is the FWHM of the (00l) ω scan and b_s is the length of the screw TD Burgers vector. The estimation does not consider edge-type dislocations and tends to overcount the screw dislocation density. The results for ammonothermal c-plane GaN are listed in Table I. All samples we measured should have dislocation density lower than 10^7 cm^{-2}. We also perform x-ray reciprocal-lattice mapping on the epilayer samples. The results confirm that the epilayers have the same orientation as the substrates and do not show significant broadenings or splittings that correspond to a large change in lattice constant or mosaic spread compared with the substrates.

We further utilize the cathodoluminescence to estimate the TD density ρ in GaN [100]. The low coordinated bonds in the dislocation core induce a one-dimensional band that is split off from the valence or conduction band; this split-off band is partially filled with majority carriers, causing band bending around the dislocation. This makes the dislocation an attractive site for minority carriers and nonradiative recombination [101]. In homoepitaxial c-plane GaN and ^{71}GaN layers, the TDs appear as dark spots and can be relatively easily visualized and counted. A representative CL image of ^{71}GaN epilayer KMiF2 is shown in Fig. 2(d) which has the highest ρ among all samples measured. The TDs in each sample are counted in three different regions with an area of $32 \times 40\,\mu$m and the largest ρ of the three regions is listed in Table II. For most of the epilayer samples the ρ is on the order of 10^6 cm^{-2}. In m-plane epilayers, we observe long dark lines that may result from parallel step edges or from subsurface screw dislocations; these features create large uncertainties in our measurements of the dislocation density. In most bulk GaN and SiC samples, the ρ is too small to determine with good accuracy using CL. (Sample KM6 is an exception, see Table I.)

The Raman spectra of bulk GaN samples are shown in Fig. 3. The strong A_1(LO) peak at 734 cm^{-1} [102] in c-plane GaN and the strong A_1(TO) peak at 531 cm^{-1} in m-plane GaN agree with the expected frequencies and selection rules [103] for a backscattering geometry [104]. The appearance of the weak, usually forbidden, A_1(TO) mode in c-plane GaN and E_1(LO) mode in m-plane GaN is a result of mixing of A_1 and E_1 modes when the incident or scattered light is not strictly parallel or perpendicular to the optical axes due the finite solid angle of the collecting objective lens [105,106]. The Raman spectra of the GaN homoepitaxial layers are not shown because we cannot easily separate the signal generated by the homoepitaxial layer from the signal generated by the substrate [107].

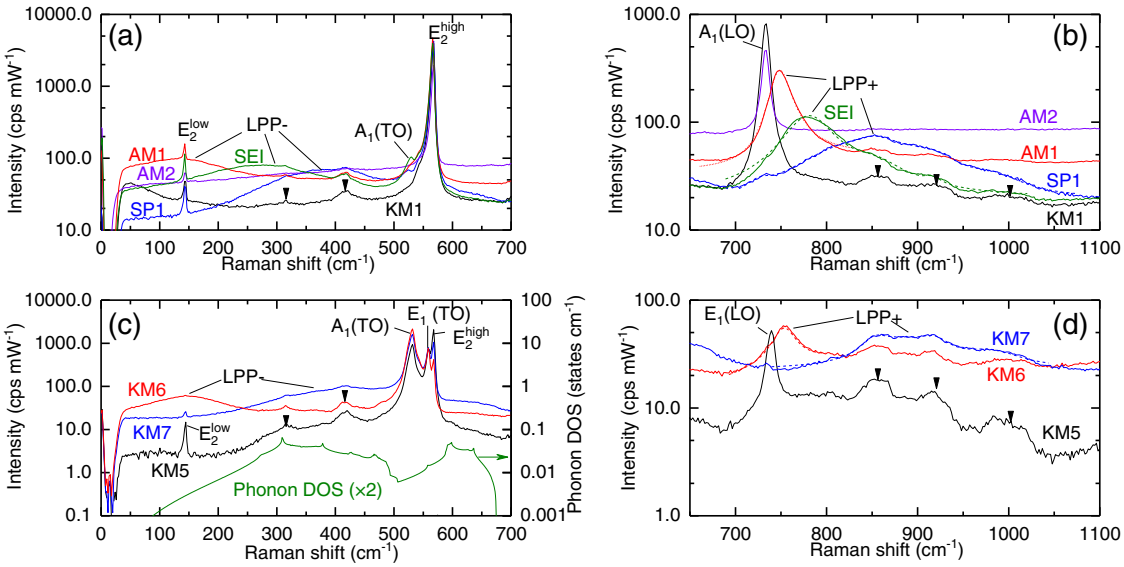

FIG. 3. Raman spectra of bulk c-plane (a), (b), and m-plane (c), (d) GaN in the low- and high-frequency range. The acoustic and optical combination modes for GaN are labeled by black triangles. The representative peak fittings of the LPP+ modes are shown in (b) and (d). The first-principles calculated phonon density of states (DOS) with frequency expanded by a factor of 2 is included in (c) for comparison.

SiC polytypes exhibit a number of distinct folded modes in the one-phonon Raman spectra of the TA and TO phonons (Fig. 4) which can be explained by folding of the Brillouin zone relative to 3C-SiC [108,109]. For these modes, we follow the definition in the literature: phonons with atomic motion parallel or perpendicular to the c axis are designated "axial" or "planar," e.g., axial acoustic mode = AA [110,111]. The frequencies of LO and folded one-phonon Raman modes labeled in Fig. 4 agree with literature values within 2 cm^{-1} [110,111]. The background from 200 to 1200 cm^{-1} in the Raman spectra is also in good agreement with the first-principles calculated phonon DOS [56] with the frequency multiplied by 2. This suggests that the Raman background is correlated with two-acoustic phonon scattering, consistent with [110]. Since phonon-plasmon coupling is not included in the calculation of the phonon DOS, it also implies that these samples have low carrier concentration. The calculated phonon DOS in GaN, Fig. 3(c), also matches the background in the Raman spectrum of the semi-insulating sample KM5, which implies a low carrier concentration in KM5 compared with other samples. The frequencies of the combination modes in GaN samples are also in agreement with the expanded phonon DOS.

We also use Raman spectroscopy to estimate the carrier concentration in bulk GaN and SiC. In these polar semiconductors [112], collective excitations of free carriers (plasmons) interact with the polar longitudinal optical phonons giving rise to Raman-active coupled longitudinal phonon-plasmon (LPP) modes [112–114]. The LPP modes comprise upper (LPP+) and lower (LPP–) branches which are above and below the uncoupled LO phonon frequency. With increasing carrier concentration, the LPP+ mode shifts to higher frequencies, broadens, and weakens in intensity. The dielectric function includes contributions from plasmons and phonons [102,115–117]:

$$\varepsilon(\omega) = \varepsilon_\infty \left(1 + \frac{\omega_L^2 - \omega_T^2}{\omega_T^2 - \omega^2 - i\omega\Gamma} - \frac{\omega_p^2}{\omega(\omega + i\gamma)}\right) \qquad (2)$$

where ω_T and ω_L are the uncoupled A_1(TO) and A_1(LO) frequencies, for c-plane GaN and c-plane SiC, and E_1(TO) and E_1(LO) frequencies for m-plane GaN, respectively. ε_∞ is the high-frequency dielectric constant, Γ is the phonon damping constant, γ is the plasmon damping constant, and

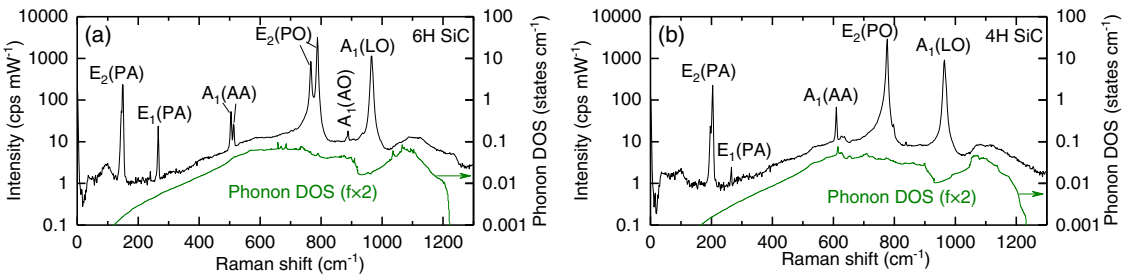

FIG. 4. Raman spectra of the (a) 4H and (b) 6H SiC. The corresponding first-principles calculated phonon density of states with frequency expanded by a factor of 2 is included for comparison.

ω_P is the plasmon frequency, given by

$$\omega_p^2 = \frac{4\pi n_R e^2}{\varepsilon_\infty m^*} \quad (3)$$

where m^* is the band-edge effective mass of the electron and n_R is the free-carrier concentration. For GaN, $\varepsilon_\infty = 5.23$ and $m^* = 0.2m_e$ [118–120]. The positions of the LPP frequencies are the roots of the equation $\varepsilon(\omega) = 0$. To simplify the calculation, we neglect the damping terms [30,117,119], and obtain

$$\omega_{\mathrm{LPP}\pm}^2 = \tfrac{1}{2}\left\{\left(\omega_L^2 + \omega_p^2\right) \pm \left[\left(\omega_L^2 + \omega_p^2\right)^2 - 4\omega_T^2\omega_p^2\right]^{1/2}\right\}. \quad (4)$$

For N-type GaN, we fit the experimental LPP+ modes with Lorentz functions with the weak combination modes considered [see dashed lines in Figs. 3(b) and 3(d)]. The carrier concentration is then estimated using $\omega_{\mathrm{LPP}+}$ and Eq. (4) to solve for ω_P. The results of $\omega_{\mathrm{LPP}\pm}$ versus n_R for the N-type samples are plotted in Fig. S3 in Supplemental Material [70], where the solution is compared with the model curves. n_R values are also summarized in Table I. They are comparable with the values obtained from the Hall effect measurements done on similar samples from the suppliers. The LPP modes derived from the Raman data show agreement with the calculated model curve, serving as a check of the validity of Eq. (4). In P-type GaN (KM1), due to the heavy damping of the hole plasmon, the coupling between the LO phonons and the plasmons is relatively insensitive to the carrier concentration [121].

For SiC, the position and shape of the A_1(LO) peak at $\approx$964 cm^{-1} in 4H and 6H SiC (Fig. 4) indicate weak LPP coupling and confirm the relatively low carrier concentration ($<10^{18}$ cm^{-3}) in these samples based on comparison with the literature [110,122]. Thus, we are unable to use Eq. (4) to estimate the carrier concentration in our SiC samples.

The temperature-dependent Λ of bulk GaN between 150 and 850 K is shown in Fig. 5(a). For all samples with dopant and impurity concentration $<10^{19}$ cm^{-3}, the measured Λ are consistent with each other across the entire range of the temperature. At 300 K, $\Lambda \approx 200 \pm 10$ W m^{-1} K^{-1}. At 850 K, $\Lambda \approx 50$ W m^{-1} K^{-1} in sample AM1 and SEI. The difference between Λ of c-plane and m-plane bulk GaN is less than the experimental uncertainties. Thus, we do not distinguish Λ_{in} and Λ_{out} in the plot.

Relatively low Λ was found in sample XYZ with high O impurity concentration and in sample AM2 with high Mn, O, and H doping. High O impurity concentration is known to reduce Λ in ammonothermal GaN [29,36]. A recent theoretical calculation pointed out that in addition to phonon scattering by O impurities and the doping induced free carriers the associated compensating Ga vacancy may also play an important role in reducing Λ [40]. Mn atoms in GaN tend to form substitutional Mn-N-Mn bonded embedded clusters [123] and distort the lattice [124], which may also strongly scatter phonons.

The consistent results for samples with different carrier type and concentrations but similar dislocation densities (e.g., samples KM5–7) suggest that the phonon scattering by free carrier densities of $<10^{18}$ cm^{-3} and the corresponding dopants are not important in reducing the Λ. Although HVPE

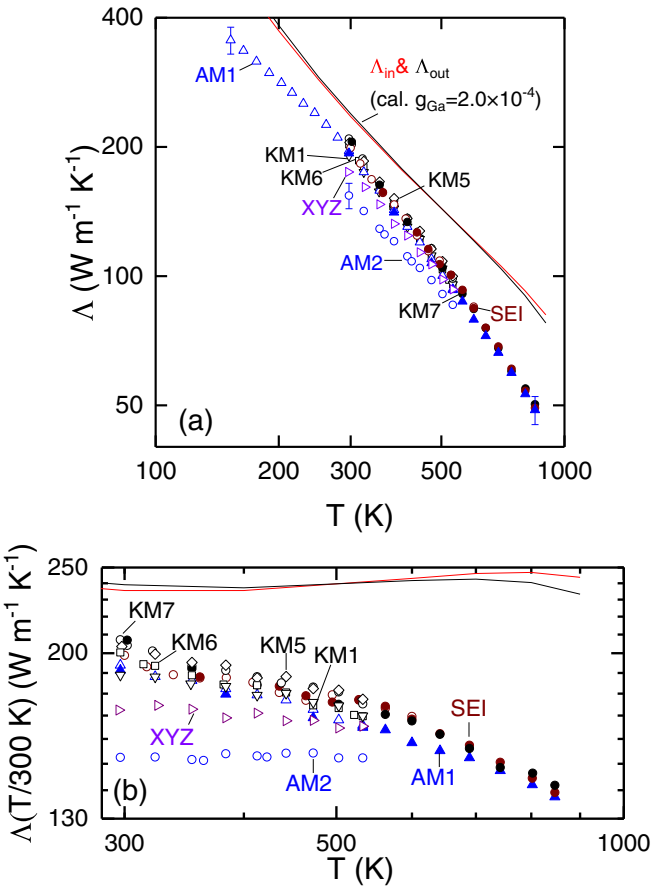

FIG. 5. (a) Thermal conductivity of bulk GaN from 150 to 850 K measured with TDTR using $1/e^2$ laser spot size $w_0 \approx 10.2\,\mu$m. The first-principles BTE calculation of Λ_{in} and Λ_{out} including three-phonon and phonon-isotope scattering of GaN (mass-disorder parameters $g_{\mathrm{Ga}} = 2.0 \times 10^{-4}$, solid lines) is presented for comparison. (b) Same thermal conductivity data as in (a), multiplied by temperature and divided by 300 K to highlight the deviations from a $1/T$ temperature dependence. The solid lines have the same meanings as in (a). In both (a) and (b), the TDTR results obtained with Al transducers are plotted as open symbols; TDTR results obtained with Pt transducers are plotted as solid symbols. Representative error bars are shown in (a).

bulk GaN samples have crystal curvature and higher dislocation density, Λ does not show a significant dependence on growth method. We conclude that when the TD density is $<10^7$ cm^{-2} the influence of TD on Λ in the bulk is weak, consistent with a previous study [34].

We plot Λ of homoepitaxial GaN and ^{71}GaN layers in Figs. 6(a) and 6(b). For all c-plane GaN epilayer samples, the Λ values are approximately the same as in bulk GaN with moderate doping, e.g., AM1, between 150 and 850 K. (See the 300-K data in Table II.) In addition, it also suggests that the application of low TD density GaN substrates with different doping and curvature does not influence the Λ of HVPE homoepitaxial layers. The m-plane GaN epilayers, which are grown side by side with the c-plane epilayers using HVPE on m-plane substrates, show relatively low Λ. We tentatively attribute the reduction in thermal conductivity to the higher impurity incorporation rate in the m-plane

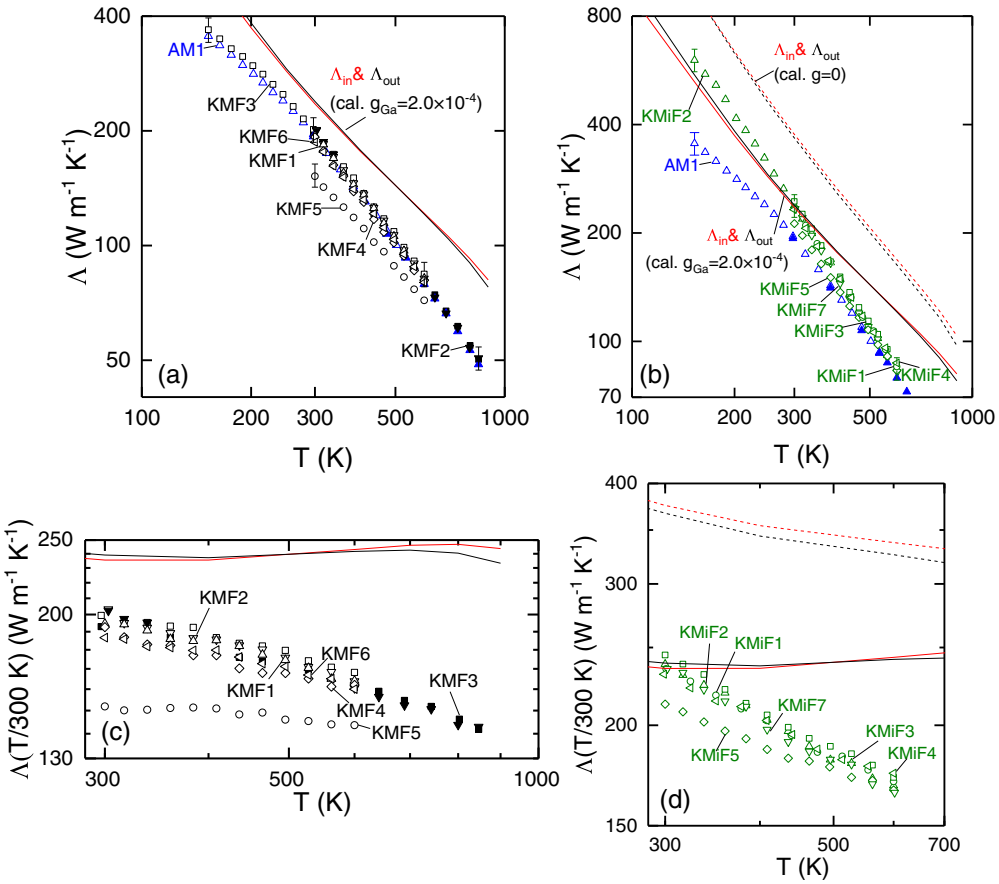

FIG. 6. (a), (b) Thermal conductivity of homoepitaxial GaN and ^{71}GaN from 150 to 850 K measured with TDTR using $1/e^2$ laser spot size $w_0 \approx 10.2\,\mu$m. The first-principles BTE calculation results of Λ_{in} and Λ_{out} including only three-phonon scattering ($g_{Ga} = 0$) [dashed lines in (b)] and three-phonon scattering combined with a total $g_{Ga} = 2.0 \times 10^{-4}$ [solid lines in (b)]. Data for the bulk sample AM1 are included for comparison. (c), (d) Same data as in (a) and (b), respectively, multiplied by temperature and divided by 300 K [solid and dashed lines have the same meanings as in (a) and (b)]. In all panels, the TDTR results obtained with Al transducers are plotted as open symbols while results obtained with Pt transducers are plotted as solid symbols. Representative error bars are shown in (a) and (b).

homoepitaxial growth compared with c-plane growth, which can lead to two-orders-of-magnitude higher O impurity concentration (reaching high 10^{19} cm^{-3}) and higher concentrations of Si impurities [125]. We note that the bulk m-plane GaN is cut from the same boule as the c-plane bulk rather than grown along the m-plane direction directly.

For the ^{71}GaN epilayer at 300 K, Λ is ≈15% higher than GaN (Table II). The experimental value for the isotope effect is therefore much smaller than the predicted 50–65% enhancement at 300 K [38,39]. We used secondary ion mass spectroscopy to characterize the impurity concentration in the ^{71}GaN layer and found a relatively high concentration of Al impurities, 1.5×10^{18} cm^{-3}, a spatially varying O concentration (≈10^{17}–10^{18} cm^{-3}), and residual ^{69}Ga between 0.1 and 1 at.% of the total Ga (data not shown). The higher TD density in the ^{71}GaN epilayers compared with the GaN epilayer may also have some effect on reducing Λ, but it should be weak considering the consistent values of Λ in ^{71}GaN with different TD densities (Table II). Similar to the m-plane GaN epilayer, the m-plane and a-plane epilayers of ^{71}Ga have lower Λ, presumably due to the higher incorporation rate of impurities for HVPE growth along these crystallographic directions.

The results of first-principles BTE calculations of Λ_{in} and Λ_{out} including three-phonon and mass-disorder phonon scattering [96] are shown in Figs. 5 and 6. The calculated Λ has weak anisotropy, with the difference between Λ_{in} and Λ_{out} of less than 5% at >300 K, consistent with the experimental data and previous first-principles calculations [34,35]. We used the general form for the isotope disorder scattering in our calculation based on Tamura's mass variation approximation as formulated in Eqs. (1), (3), and (4) of [96]. The mass-disorder phonon scattering rate is proportional to the parameter

$$g_\sigma = \sum_i f_i(\sigma)\left(1 - \frac{M_i(\sigma)}{\overline{M}(\sigma)}\right)^2 \qquad (5)$$

where $M_i(\sigma)$ and $f_i(\sigma)$ are the atomic mass and atomic fraction of the ith atom at site σ and $\overline{M}(\sigma)$ is the average mass of the σ site atom, $\overline{M}(\sigma) = \sum_i f_i(\sigma) M_i(\sigma)$.

In GaN with natural isotope abundance, the mass-disorder parameters are $g_{Ga} = 2.0 \times 10^{-4}$ and $g_N = 1.8 \times 10^{-5}$. The much larger value of g_{Ga} compared to g_N stems from the large isotope mix on the Ga atoms (60.11% ^{69}Ga and 39.89% ^{71}Ga)

while N atoms are 99.64% ^{14}N. Including g_N has negligible effect on Λ since it only slightly affects the N atoms which has negligible effect on changing the heat-carrying acoustic phonons due to the large Ga to N mass ratio. We consider only g_{Ga} in the BTE calculations for natural GaN.

The room-temperature experimental Λ of natural samples with low doping and impurity concentrations ($\approx$200 W m^{-1} K^{-1}) is $\approx$15% smaller than the BTE calculation for GaN with natural isotope mix on the Ga atoms ($g_{Ga} = 2.0 \times 10^{-4}$). More importantly, the measured Λ has a much stronger temperature dependence than predicted by theory. On average, $\Lambda \propto T^{-1.2}$ in the range $300 < T < 600$ K and $\Lambda \propto T^{-1.5}$ in the range $600 < T < 850$ K. The temperature dependence above the Debye temperature in GaN ($\Theta_D \approx 636$ K [126]) is weaker than that in AlN, which has $\Lambda \propto T^{-1.7}$ [127]. For the ^{71}GaN epilayer, the measured Λ is 35% smaller than the calculated prediction at 300 K [Fig. 6(b)], which is expected considering the large amount of impurities in the ^{71}GaN samples. Adding a mass disorder scattering with $g_{Ga} = 2.0 \times 10^{-4}$ in the calculation reduces the difference near 300 K but causes an even larger difference in the slope of the temperature dependence between the calculation and experiment. In addition, resonant phonon-impurity scattering, which typically causes a dip at well below the Debye temperature and suppresses the Λ, should also lead to weaker temperature dependence in dielectric crystals at relatively high temperature as has been shown in many prior works [37,128–130]. This suggests that phonon scattering mechanisms other than scattering by residual isotopes and other impurities may need to be considered.

In Figs. 5(b), 6(c), and 6(d), we plot the measured Λ scaled by temperature and divided by 300 K, i.e., $\Lambda(T/300\,\mathrm{K})$, to compress the range of the data and more clearly present the differences between theory and experiment. In these figures, a $\Lambda \propto T^{-1}$ dependence would appear as a horizontal line. The slopes of our experimental data are steeper than the typical high-temperature three-phonon limited scattering T^{-1} behavior of insulating crystals, which is expected for temperatures above approximately one-half of the Debye temperature [131]. The more rapid rise than T^{-1} seen in the measured data below 600 K is in part a consequence of the decrease in resistive umklapp scattering which gives a steeper temperature dependence. At >600 K, on the other hand, the slope of the experimental data increases further ($\Lambda \propto T^{-1.5}$), which is significantly different from the relatively flat theoretical curve.

We attribute this result to possible significant contributions from four-phonon scattering processes to the thermal conductivity of GaN. In GaN, the large frequency gap ($\approx$6 THz) between the acoustic and optic phonon branches, and the high phonon frequency scale, lead to unusually weak anharmonic three-phonon scattering between acoustic and optic phonons in a narrow frequency range [39,132,133], as seen in the sharp dip in three-phonon scattering rates in the 5–7-THz range at 300 K (see Fig. S4 in Supplemental Material [70]; also shown in Fig. S4 are the phonon-isotope scattering rates). Note that the phonon-isotope scattering rates are comparable to the three-phonon scattering rates in the region of the dip, thus strongly suppressing the three-phonon limited Λ. Figure S5 in Supplemental Material shows the main spectral contributions to Λ for isotopically pure GaN (red curve) and GaN with natural isotope mixture (blue curve) at 300 K. Note the sharp peak in contributions for the isotopically pure case in the 5–7-THz range, which is strongly suppressed by phonon-isotope scattering. This suggests that four-phonon scattering should be more important for isotopically pure ^{71}GaN than for natural GaN. This conclusion is consistent with the larger differences between measured and calculated Λ for the latter case, although the relatively higher impurity concentrations in ^{71}GaN compared to natural GaN may also suppress the measured Λ in ^{71}GaN slightly.

Four-phonon scattering has been predicted to play a role in determining the thermal conductivity in Si and Ge at high temperature [134]. In zinc-blende structured boron arsenide (BAs), which also have weak three-phonon scattering due in part to the large frequency gap between acoustic and optic phonons, four-phonon scattering processes have a strong effect on suppressing Λ above 200 K, because the phonon frequency gap limits three-phonon scattering but does not restrict the phase space of the four-phonon scattering [135–137]. At 300 K, the predicted Λ from a calculation including three-phonon, four-phonon, and phonon-isotope scattering, 1260 W m^{-1} K^{-1}, is about half that obtained without four-phonon scattering (2330 W m^{-1} K^{-1}), and is close to the experimentally measured values [137]. In the high-temperature limit, the four-phonon scattering rate τ_4^{-1} is expected to scale with T^2, giving rise to a stronger temperature dependence of Λ than the T^{-1} dependence expected when three-phonon scattering is dominant [134]. The increasingly steep temperature dependence of the measured Λ at elevated temperatures suggests that four-phonon scattering is important in GaN, and that inclusion of higher-order phonon scattering processes in the first-principles calculations for GaN may be necessary.

The Λ and the scaled $\Lambda(T/300\,\mathrm{K})$ of 4H and 6H SiC between 300 and 850 K are shown in Fig. 7. Across the full temperature range, 4H SiC shows higher Λ than 6H SiC; for both polytypes, Λ_{in} is larger than Λ_{out}, consistent with previous studies [54,56]. At 300 K, $\Lambda_{out} = 345$ and 320 W m^{-1} K^{-1}; at 850 K, $\Lambda_{out} = 85$ and 78 W m^{-1} K^{-1} for 4H and 6H SiC, respectively. At 300 K, $\Lambda_{in} = 415$ and 390 W m^{-1} K^{-1}; at 600 K, $\Lambda_{in} = 150$ and 140 W m^{-1} K^{-1} for 4H and 6H SiC, respectively. (We fitted the measured Λ of GaN and both 4H and 6H SiC with an empirical equation for engineering usage in Table SI in Supplemental Material [70].) The Debye temperature of SiC is high, $\Theta_D \approx 1200$ K [49]. Thus, Λ of SiC shows a change of slope at $T < 600$ K in these log-log plots due to the onset of exponential temperature dependence of umklapp scattering rates at low temperatures. At $600 < T < 850$ K, $\Lambda \propto T^{-1.2}$ and $\Lambda \propto T^{-1.1}$ for 4H and 6H SiC, respectively, which is less rapid compared with $\Lambda \propto T^{-1.5}$ in GaN in this temperature range. This can also be seen in the relatively flat curve at high temperature in Fig. 7(c) compared with Figs. 5(b), 6(b), and 6(c). Across the temperature range 300 to 850 K, Λ of GaN is 60–70% of the value of thermal conductivity of 4H and 6H SiC. This suggests that SiC is more advantageous than GaN in terms of thermal management in high power devices and special devices for aircraft and spacecraft applications operating at high ambient

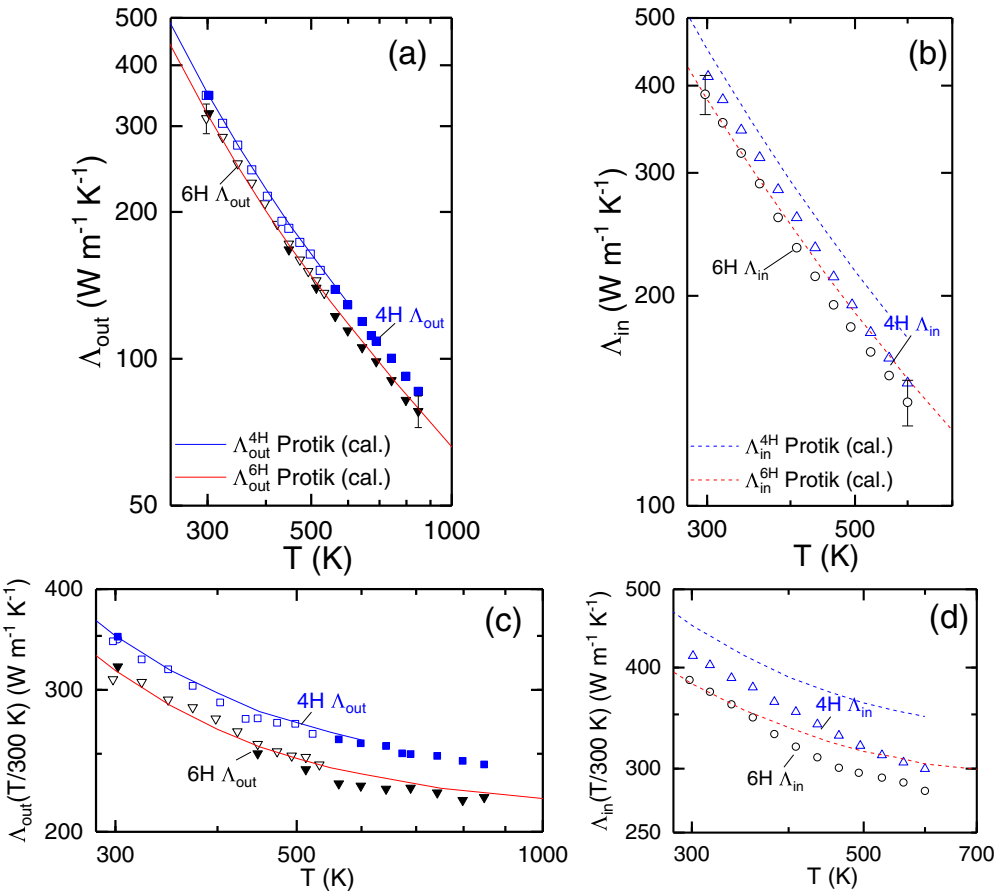

FIG. 7. (a), (b) Thermal conductivity of 4H and 6H SiC along in- and out-of-plane directions from 300 to 850 K measured with TDTR using $1/e^2$ laser spot size $w_0 \approx 10.2\,\mu$m. The first-principles BTE calculations from [56] are shown for comparison. (c), (d) The same data as plotted in (a) and (b), respectively, multiplied by temperature and divided by 300 K. Solid and dashed lines have the same meaning as in (a) and (b). Representative error bars are shown in (a) and (b).

temperature. Note that other factors, especially the electronic properties of SiC and GaN as well as the design of the power dissipated inside the device and the cooling system, need to be considered to determine the thermal stability and ultimate performance of a real device.

Data for 4H and 6H SiC show good agreement with the predictions of first-principles BTE calculations that consider only three-phonon scattering [56]. At the L point in the Brillouin zone, the gap between the highest-frequency acoustic phonons and the lowest-frequency optical phonons in hexagonal SiC is ≈4 THz. This gap is significantly smaller than in GaN (6 THz at the M point). The smaller gap in SiC is expected to lead to stronger three-phonon scattering in SiC than in GaN in the frequency region that gives the largest contribution to Λ. The agreement between experiment and theory is better for Λ_{out} than for Λ_{in}, especially for 4H SiC. We speculate that there is a greater importance of four-phonon scattering in the in-plane direction relative to the out-of-plane direction which is not captured in the calculation [56].

IV. CONCLUSION

In GaN substrates and epilayers with a low dislocation density ($<10^7$ cm^{-2}) and doping and impurity concentration, the thermal conductivity is nearly isotropic without observable dependence on the exact dislocation and doping conditions. In ^{71}GaN epilayers, the measured Λ at 300 K is approximately 15% higher than GaN with natural isotope abundance which is smaller than the isotope effect predicted by first-principles calculations. The measured Λ of 4H and 6H SiC is 60–70% larger than that of GaN at all temperatures, which suggests that SiC is advantageous for thermal management of high-power devices even at elevated temperatures. A comparison between the measurement results and our first-principles calculations shows that the temperature dependence of Λ in GaN is significantly stronger than the prediction considering only three-phonon scattering, while the agreement in SiC is relatively good. These results combined with the calculated unusually weak three-phonon scattering indicate the possible importance of higher-order phonon scattering in determining the thermal conductivity of GaN particularly for ^{71}GaN. This paper provides benchmark knowledge about the thermal transport properties and the wide-band-gap semiconductors of GaN, ^{71}GaN, and SiC especially in the high-temperature range and contributes to the understanding of phonon scattering mechanism in these materials.

ACKNOWLEDGMENTS

We acknowledge financial support from US Department of Energy ARPA-E Project No. DE-AR0000876 through the PNDIODES program administered by Dr. Isik Kizilyalli. TDTR, XRD, Raman, and CL were carried out, in part, in the Frederick Seitz Materials Research Laboratory Central Research Facilities, University of Illinois. C.L. and D.B. also acknowledge support from ONR under Multidisciplinary University Research Initiative Grant No. N00014-16-1-2436 and from the Boston College Linux Cluster.

[1] H. Amano, Y. Baines, E. Beam, M. Borga, T. Bouchet, P. R. Chalker, M. Charles, K. J. Chen, N. Chowdhury, R. Chu *et al.*, J. Phys. D **51**, 163001 (2018).

[2] F. Roccaforte, P. Fiorenza, G. Greco, R. Lo Nigro, F. Giannazzo, F. Iucolano, and M. Saggio, Microelectron. Eng. **187-188**, 66 (2018).

[3] I. C. Kizilyalli, Y. A. Xu, E. Carlson, J. Manser, and D. W. Cunningham, in Proceedings of the Fifth IEEE Workshop on Wide Bandgap Power Devices and Applications (WiPDA), 2017 (unpublished), p. 417.

[4] D. Garrido-Diez and I. Baraia, in Proceedings of the IEEE International Workshop of Electronics, Control, Measurement, Signals and their Application to Mechatronics (ECMSM), 2017 (unpublished), p. 1.

[5] M. Andresen and M. Liserre, Microelectron. Reliab. **54**, 1935 (2014).

[6] C. E. Green, A. G. Fedorov, and Y. K. Joshi, IEEE Trans. Compon. Packag. Technol. **32**, 868 (2009).

[7] A. L. Moore and L. Shi, Mater. Today **17**, 163 (2014).

[8] N. Killat *et al.*, IEEE Electron Device Letters **33**, 366 (2012).

[9] J. K. Hite, T. J. Anderson, L. E. Luna, J. C. Gallagher, M. A. Mastro, J. A. Freitas, and C. R. Eddy, J. Cryst. Growth **498**, 352 (2018).

[10] A. Balachandran, H. Song, T. S. Sudarshan, and M. V. S. Chandrashekhar, J. Cryst. Growth **448**, 97 (2016).

[11] I. C. Kizilyalli, A. P. Edwards, O. Aktas, T. Prunty, and D. Bour, IEEE Trans. Electron Devices **62**, 414 (2015).

[12] D. Disney, H. Nie, A. Edwards, D. Bour, H. Shah, I. C. Kiziyalli, and Q. Jiang, in Proceedings of the 26th IEEE International Symposium on Power Semiconductor Devices and IC's (ISPSD), 2014 (unpublished), p. 1.

[13] H. Nie *et al.*, IEEE Electron Device Lett. **35**, 939 (2014).

[14] K. Fujito, S. Kubo, H. Nagaoka, T. Mochizuki, H. Namita, and S. Nagao, J. Cryst. Growth **311**, 3011 (2009).

[15] M. Bockowski, M. Iwinska, M. Amilusik, M. Fijalkowski, B. Lucznik, and T. Sochacki, Semicond. Sci. Technol. **31**, 093002 (2016).

[16] C. Hennig, E. Richter, U. Zeimer, M. Weyers, and G. Tränkle, Phys. Status Solidi C **3**, 1466 (2006).

[17] H. M. Foronda, A. E. Romanov, E. C. Young, C. A. Robertson, G. E. Beltz, and J. S. Speck, J. Appl. Phys. **120**, 035104 (2016).

[18] K. Yamane, T. Matsubara, T. Yamamoto, N. Okada, A. Wakahara, and K. Tadatomo, J. Appl. Phys. **119**, 045707 (2016).

[19] S. Suihkonen, S. Pimputkar, S. Sintonen, and F. Tuomisto, Adv. Electron. Mater. **3**, 1600496 (2017).

[20] M. Zajac *et al.*, Prog. Cryst. Growth Charact. Mater. **64**, 63 (2018).

[21] D. Ehrentraut and T. Fukuda, Proc. IEEE **98**, 1316 (2010).

[22] S. Sakari, S. Sami, J. Henri, D. Andreas, S. Romuald, O. T. Turkka, and L. Harri, Appl. Phys. Express **7**, 091003 (2014).

[23] P. Wellmann, G. Neubauer, L. Fahlbusch, M. Salamon, and N. Uhlmann, Cryst. Res. Technol. **50**, 2 (2015).

[24] H. Shibata *et al.*, Mater. Trans. **48**, 2782 (2007).

[25] G. A. Slack, L. J. Schowalter, D. Morelli, and J. A. Freitas, J. Cryst. Growth **246**, 287 (2002).

[26] A. Jeżowski, B. A. Danilchenko, M. Boćkowski, I. Grzegory, S. Krukowski, T. Suski, and T. Paszkiewicz, Solid State Commun. **128**, 69 (2003).

[27] P. P. Paskov, M. Slomski, J. H. Leach, J. F. Muth, and T. Paskova, AIP Advances **7**, 095302 (2017).

[28] W. Liu, A. A. Balandin, C. Lee, and H.-Y. Lee, Phys. Status Solidi A **202**, R135 (2005).

[29] A. Jeżowski, O. Churiukova, J. Mucha, T. Suski, I. A. Obukhov, and B. A. Danilchenko, Mater. Res. Express **2**, 085902 (2015).

[30] D. I. Florescu, V. M. Asnin, F. H. Pollak, R. J. Molnar, and C. E. C. Wood, J. Appl. Phys. **88**, 3295 (2000).

[31] V. Asnin, F. H. Pollak, J. Ramer, M. Schurman, and I. Ferguson, Appl. Phys. Lett. **75**, 1240 (1999).

[32] C.-Y. Luo, H. Marchand, D. Clarke, and S. DenBaars, Appl. Phys. Lett. **75**, 4151 (1999).

[33] C. Luo, D. Clarke, and J. Dryden, J. Electron. Mater. **30**, 138 (2001).

[34] T. E. Beechem, A. E. McDonald, E. J. Fuller, A. A. Talin, C. M. Rost, J.-P. Maria, J. T. Gaskins, P. E. Hopkins, and A. A. Allerman, J. Appl. Phys. **120**, 095104 (2016).

[35] C. Mion, J. F. Muth, E. A. Preble, and D. Hanser, Appl. Phys. Lett. **89**, 092123 (2006).

[36] R. B. Simon, J. Anaya, and M. Kuball, Appl. Phys. Lett. **105**, 202105 (2014).

[37] R. Rounds, B. Sarkar, T. Sochacki, M. Bockowski, M. Imanishi, Y. Mori, R. Kirste, R. Collazo, and Z. Sitar, J. Appl. Phys. **124**, 105106 (2018).

[38] R. Wu, R. Hu, and X. Luo, J. Appl. Phys. **119**, 145706 (2016).

[39] L. Lindsay, D. A. Broido, and T. L. Reinecke, Phys. Rev. Lett. **109**, 095901 (2012).

[40] A. Katre, J. Carrete, T. Wang, G. K. H. Madsen, and N. Mingo, Phys. Rev. Mater. **2**, 050602 (2018).

[41] M. Asen-Palmer, K. Bartkowski, E. Gmelin, M. Cardona, A. P. Zhernov, A. V. Inyushkin, A. Taldenkov, V. I. Ozhogin, K. M. Itoh, and E. E. Haller, Phys. Rev. B **56**, 9431 (1997).

[42] A. V. Inyushkin, A. N. Taldenkov, A. M. Gibin, A. V. Gusev, and H. J. Pohl, Phys. Status Solidi C **1**, 2995 (2004).

[43] A. V. Inyushkin, A. N. Taldenkov, J. W. Ager, E. E. Haller, H. Riemann, N. V. Abrosimov, H.-J. Pohl, and P. Becker, J. Appl. Phys. **123**, 095112 (2018).

[44] T. H. Geballe and G. W. Hull, Phys. Rev. **110**, 773 (1958).

[45] J. R. Olson, R. O. Pohl, J. W. Vandersande, A. Zoltan, T. R. Anthony, and W. F. Banholzer, Phys. Rev. B **47**, 14850 (1993).

[46] T. R. Anthony, W. F. Banholzer, J. F. Fleischer, L. Wei, P. K. Kuo, R. L. Thomas, and R. W. Pryor, Phys. Rev. B **42**, 1104 (1990).

[47] P. Waltereit, O. Brandt, A. Trampert, H. T. Grahn, J. Menniger, M. Ramsteiner, M. Reiche, and K. H. Ploog, Nature (London) **406**, 865 (2000).

[48] F. Bernardini and V. Fiorentini, Phys. Rev. B **57**, R9427 (1998).

[49] G. A. Slack, J. Appl. Phys. **35**, 3460 (1964).

[50] D. T. Morelli, J. P. Heremans, C. P. Beetz, W. S. Yoo, and H. Matsunami, Appl. Phys. Lett. **63**, 3143 (1993).

[51] D. Morelli, J. Heremans, C. Beetz, W. Woo, G. Harris, and C. Taylor, in *Institute of Physics Conference Series* (Hilger, London, 1994), p. 313.

[52] R. Wei, S. Song, K. Yang, Y. Cui, Y. Peng, X. Chen, X. Hu, and X. Xu, J. Appl. Phys. **113**, 053503 (2013).

[53] E. Ziade, J. Yang, G. Brummer, D. Nothern, T. Moustakas, and A. J. Schmidt, Appl. Phys. Lett. **107**, 091605 (2015).

[54] X. Qian, P. Jiang, and R. Yang, Mater. Today Phys. **3**, 70 (2017).

[55] S. G. Müller, R. Eckstein, J. Fricke, D. Hofmann, R. Hofmann, R. Horn, H. Mehling, and O. Nilsson, Mater. Sci. Forum **264-268**, 623 (1997).

[56] N. H. Protik, A. Katre, L. Lindsay, J. Carrete, N. Mingo, and D. Broido, Mater. Today Physics **1**, 31 (2017).

[57] E. A. Burgemeister, W. von Muench, and E. Pettenpaul, J. Appl. Phys. **50**, 5790 (1979).

[58] H. Nykänen, P. Mattila, S. Suihkonen, J. Riikonen, E. Quillet, E. Homeyer, J. Bellessa, and M. Sopanen, J. Appl. Phys. **109**, 083105 (2011).

[59] Q. Zheng, Ph.D. dissertation, University of Illinois at Urbana-Champaign, 2017.

[60] D. G. Cahill, Rev. Sci. Instrum. **75**, 5119 (2004).

[61] K. Kang, Y. K. Koh, C. Chiritescu, X. Zheng, and D. G. Cahill, Rev. Sci. Instrum. **79**, 114901 (2008).

[62] J. Yang, E. Ziade, and A. J. Schmidt, Rev. Sci. Instrum. **87**, 014901 (2016).

[63] R. B. Wilson and D. G. Cahill, Nat. Commun. **5**, 5075 (2014).

[64] R. B. Wilson and D. G. Cahill, Appl. Phys. Lett. **107**, 203112 (2015).

[65] D. G. Cahill and F. Watanabe, Phys. Rev. B **70**, 235322 (2004).

[66] P. D. Desai, H. M. James, and C. Y. Ho, J. Phys. Chem. Ref. Data **13**, 1131 (1984).

[67] E. H. Buyco and F. E. Davis, J. Chem. Eng. Data **15**, 518 (1970).

[68] J. W. Arblaster, Johnson Matthey Technol. Rev. **59**, 174 (2015).

[69] J. Arblaster, Platinum Met. Rev. **38**, 119 (1994).

[70] See Supplemental Material at http://link.aps.org/supplemental/10.1103/PhysRevMaterials.3.014601 for heat capacity and spot size dependent thermal conductivity data, phonon plasmon coupling mode frequencies from Raman, and further information about the first-principles calculation.

[71] T. Tsuchiya, K. Kawamura, O. Ohtaka, H. Fukui, and T. Kikegawa, Solid State Commun. **121**, 555 (2002).

[72] *Group IV Elements, IV-IV and III-V Compounds. Part A: Lattice Properties*, edited by O. Madelung, U. Rössler, and M. Schulz (Springer, New York, 2001), p. 1.

[73] C. Roder, S. Einfeldt, S. Figge, and D. Hommel, Phys. Rev. B **72**, 085218 (2005).

[74] Z. Li and R. C. Bradt, J. Appl. Phys. **60**, 612 (1986).

[75] Z. Li and R. C. Bradt, J. Am. Ceram. Soc. **69**, 863 (1986).

[76] R. K. Kremer, M. Cardona, E. Schmitt, J. Blumm, S. K. Estreicher, M. Sanati, M. Bockowski, I. Grzegory, T. Suski, and A. Jezowski, Phys. Rev. B **72**, 075209 (2005).

[77] O. Nilsson, H. Mehling, R. Horn, J. Fricke, R. Hofmann, S. G. Müller, R. Eckstein, and D. Hofmann, High Temperatures–High Pressures **29**, 73 (1997).

[78] L. Hitova, R. Yakimova, E. Trifonova, A. Lenchev, and E. Janzén, J. Electrochem. Soc. **147**, 3546 (2000).

[79] M. Chase, Jr., C. Davies, J. Downey, Jr., D. Frurip, R. Mc Donald, and A. Syverud, J. Phys. Chem. Ref. Data **14**, 635 (1985).

[80] Y. Touloukian and E. Buyco, *Thermophysical Properties of Matter: The TPRC Data Series*, Specific Heat–Nonmetallic Solids Vol. 5 (Plenum Publishing Corporation, New York, 1970).

[81] V. Kirillin, A. Sheindlin, and V. Y. Chekhovskoi, in *Refractory Carbides* (Springer, New York, 1974), p. 353.

[82] L. V. Gurvich and I. Veyts, *Thermodynamic Properties of Individual Substances: Elements and Compounds* (Taylor & Francis, London, 1990).

[83] J. Leitner, A. Strejc, D. Sedmidubský, and K. Růžička, Thermochimica Acta **401**, 169 (2003).

[84] K. Itagaki and K. Yamaguchi, Thermochimica Acta **163**, 1 (1990).

[85] X.-l. Chen, Y.-c. Lan, J.-k. Liang, X.-r. Cheng, Y.-p. Xu, T. Xu, P.-z. Jiang, and K.-q. Lu, Chin. Phys. Lett. **16**, 107 (1999).

[86] K. Jacob, S. Singh, and Y. Waseda, J. Mater. Res. **22**, 3475 (2007).

[87] B. Danilchenko, T. Paszkiewicz, S. Wolski, A. Jeżowski, and T. Plackowski, Appl. Phys. Lett. **89**, 061901 (2006).

[88] I. Zięborak-Tomaszkiewicz, E. Utzig, and P. Gierycz, J. Therm. Anal. Calorim. **91**, 329 (2008).

[89] A. Demidenko, V. Koshchenko, L. Sabanova, and Y. M. Gran, Russ. J. Phys. Chem. A **49**, 1585 (1975).

[90] D. A. Broido, M. Malorny, G. Birner, N. Mingo, and D. A. Stewart, Appl. Phys. Lett. **91**, 231922 (2007).

[91] A. Ward, D. A. Broido, D. A. Stewart, and G. Deinzer, Phys. Rev. B **80**, 125203 (2009).

[92] G. Paolo *et al.*, J. Phys.: Condens. Matter **21**, 395502 (2009).

[93] K. F. Garrity, J. W. Bennett, K. M. Rabe, and D. Vanderbilt, Comput. Mater. Sci. **81**, 446 (2014).

[94] H. Schulz and K. Thiemann, Solid State Commun. **23**, 815 (1977).

[95] W. Li, L. Lindsay, D. A. Broido, D. A. Stewart, and N. Mingo, Phys. Rev. B **86**, 174307 (2012).

[96] S.-i. Tamura, Phys. Rev. B **30**, 849 (1984).

[97] M. A. Moram and M. E. Vickers, Rep. Prog. Phys. **72**, 036502 (2009).

[98] H. Heinke, V. Kirchner, S. Einfeldt, and D. Hommel, Appl. Phys. Lett. **77**, 2145 (2000).

[99] R. Chierchia, T. Böttcher, H. Heinke, S. Einfeldt, S. Figge, and D. Hommel, J. Appl. Phys. **93**, 8918 (2003).

[100] S. J. Rosner, E. C. Carr, M. J. Ludowise, G. Girolami, and H. I. Erikson, Appl. Phys. Lett. **70**, 420 (1997).

[101] J.-L. Farvacque, Mater. Sci. Eng. B **42**, 110 (1996).

[102] M. Kuball, Surf. Interface Anal. **31**, 987 (2001).

[103] H. Harima, J. Phys.: Condens. Matter **14**, R967 (2002).
[104] V. Y. Davydov, Y. E. Kitaev, I. N. Goncharuk, A. N. Smirnov, J. Graul, O. Semchinova, D. Uffmann, M. B. Smirnov, A. P. Mirgorodsky, and R. A. Evarestov, Phys. Rev. B **58**, 12899 (1998).
[105] L. Filippidis, H. Siegle, A. Hoffmann, C. Thomsen, K. Karch, and F. Bechstedt, Phys. Status Solidi B **198**, 621 (1996).
[106] T. Azuhata, T. Sota, K. Suzuki, and S. Nakamura, J. Phys.: Condens. Matter **7**, L129 (1995).
[107] H. Y. Zhang, X. H. He, Y. H. Shih, M. Schurman, Z. C. Feng, and R. A. Stall, Opt. Lett. **21**, 1529 (1996).
[108] D. W. Feldman, J. H. Parker, W. J. Choyke, and L. Patrick, Phys. Rev. **173**, 787 (1968).
[109] S. Nakashima and K. Tahara, Phys. Rev. B **40**, 6339 (1989).
[110] J. C. Burton, L. Sun, M. Pophristic, S. J. Lukacs, F. H. Long, Z. C. Feng, and I. T. Ferguson, J. Appl. Phys. **84**, 6268 (1998).
[111] D. W. Feldman, J. H. Parker, W. J. Choyke, and L. Patrick, Phys. Rev. **170**, 698 (1968).
[112] T. Kozawa, T. Kachi, H. Kano, Y. Taga, M. Hashimoto, N. Koide, and K. Manabe, J. Appl. Phys. **75**, 1098 (1994).
[113] A. S. Barker and M. Ilegems, Phys. Rev. B **7**, 743 (1973).
[114] Y. Peng, X. Xu, X. Hu, K. Jiang, S. Song, Y. Gao, and H. Xu, J. Appl. Phys. **107**, 093519 (2010).
[115] M. Yoon, P. Il-Woo, H. Choi, P. Sung Soo, and K. Eui Kwan, Jpn. J. Appl. Phys. **44**, 828 (2005).
[116] H. Harima, S. i. Nakashima, and T. Uemura, J. Appl. Phys. **78**, 1996 (1995).
[117] P. Perlin, J. Camassel, W. Knap, T. Taliercio, J. C. Chervin, T. Suski, I. Grzegory, and S. Porowski, Appl. Phys. Lett. **67**, 2524 (1995).
[118] S. Pezzagna, J. Brault, M. Leroux, J. Massies, and M. de Micheli, J. Appl. Phys. **103**, 123112 (2008).
[119] L. H. Robins, E. Horneber, N. A. Sanford, K. A. Bertness, M. Brubaker, and J. Schlager, J. Appl. Phys. **120**, 124313 (2016).
[120] G. Irmer, V. V. Toporov, B. H. Bairamov, and J. Monecke, Phys. Status Solidi B **119**, 595 (1983).
[121] H. Harima, T. Inoue, S. Nakashima, K. Furukawa, and M. Taneya, Appl. Phys. Lett. **73**, 2000 (1998).
[122] M. V. Klein, B. N. Ganguly, and P. J. Colwell, Phys. Rev. B **6**, 2380 (1972).
[123] X. Y. Cui, B. Delley, A. J. Freeman, and C. Stampfl, Phys. Rev. B **76**, 045201 (2007).
[124] N. Mingo, D. Hauser, N. P. Kobayashi, M. Plissonnier, and A. Shakouri, Nano Letters **9**, 711 (2009).
[125] M. Amilusik *et al.*, J. Cryst. Growth **403**, 48 (2014).
[126] K. Adachi, H. Ogi, A. Nagakubo, N. Nakamura, M. Hirao, M. Imade, M. Yoshimura, and Y. Mori, J. Appl. Phys. **119**, 245111 (2016).
[127] G. A. Slack, R. A. Tanzilli, R. O. Pohl, and J. W. Vandersande, J. Phys. Chem. Solids **48**, 641 (1987).
[128] R. O. Pohl, Phys. Rev. Lett. **8**, 481 (1962).
[129] M. Holland, Phys. Rev. **134**, A471 (1964).
[130] A. Katre, J. Carrete, B. Dongre, G. K. H. Madsen, and N. Mingo, Phys. Rev. Lett. **119**, 075902 (2017).
[131] G. Leibfried and E. Schlömann, *Wärmeleitung in Elektrisch Isolierenden Kristallen* (Vandenhoeck & Ruprecht, Göttingen, Germany, 1954).
[132] J. Garg, T. Luo, and G. Chen, Appl. Phys. Lett. **112**, 252101 (2018).
[133] X. Wu, J. Lee, V. Varshney, J. L. Wohlwend, A. K. Roy, and T. Luo, Sci. Rep. **6**, 22504 (2016).
[134] C. J. Glassbrenner and G. A. Slack, Phys. Rev. **134**, A1058 (1964).
[135] T. Feng, L. Lindsay, and X. Ruan, Phys. Rev. B **96**, 161201 (2017).
[136] S. Li, Q. Zheng, Y. Lv, X. Liu, X. Wang, P. Y. Huang, D. G. Cahill, and B. Lv, Science **361**, 579 (2018).
[137] F. Tian *et al.*, Science **361**, 582 (2018).

Correction: A power of 10 did not convert properly in Table I and has been fixed.